



Science Arts & Métiers (SAM)

is an open access repository that collects the work of Arts et Métiers Institute of Technology researchers and makes it freely available over the web where possible.

This is an author-deposited version published in: <https://sam.ensam.eu>
Handle ID: <http://hdl.handle.net/10985/19442>

To cite this version :

Houssem BEN BOUBAKER, Charles MAREAU, Yessine AYED, Guénaél GERMAIN, Fabrice GUERIN - Development of a Hyperelastic Constitutive Model Based on the Crystal Plasticity Theory for the Simulation of Machining Operations - In: 17th CIRP Conference on Modelling of Machining Operations, CIRP CMMO, Royaume-Uni, 2019-06-13 - 17th CIRP Conference on Modelling of Machining Operations, CIRP CMMO - 2019

Any correspondence concerning this service should be sent to the repository

Administrator : scienceouverte@ensam.eu



17th CIRP Conference on Modelling of Machining Operations

Development of a Hyperelastic Constitutive Model Based on the Crystal Plasticity Theory for the Simulation of Machining Operations

H.B. Boubaker^a, C.Mareau^a, Y.Ayed^a, G.Germain^a, F.Guerin^b^aArts et Métiers, Campus d'Angers, LAMPA, 2 bd du Ronceray, 49035 Angers Cedex 1, France^bEcole d'Ingénieurs de l'Université d'Angers, LARIS, Angers, France

Abstract

In this work, a hyperelastic constitutive model is developed to describe the thermo-mechanical behavior of the Ti17 titanium alloy. The grain shape and the crystallographic orientation are explicitly taken into account. The behavior of both the α and β phases is modelled with a crystal plasticity formulation coupled to a CDM (Continuum Damage Model). The constitutive model is implemented in the ABAQUS/Explicit finite element solver with a user-defined subroutine. The model parameters are identified from experimental tests. According to the cutting simulation results, both strain localization and chip segmentation are strongly impacted by the crystallographic orientation.

© 2019 The Authors. Published by Elsevier B.V.

Peer-review under responsibility of the scientific committee of The 17th CIRP Conference on Modelling of Machining Operations

Keywords: ; Numerical simulation; Crystal plasticity model; Hyperelastic formulation; Adiabatic shear bands

1. Introduction

Titanium alloys are widely used in the aerospace industry due to their high strength-to-weight ratio, combined with an excellent corrosion resistance and good mechanical properties even at high temperature. However, due to their high hardness at elevated temperatures, low thermal conductivity and high chemical reactivity[1], machining operations are often difficult for titanium alloys. Indeed, during the cutting process, the low thermal conductivity limits heat conduction, which leads to an important temperature increase of both the workpiece and the tool. As a result, plastic deformation is localized into narrow shear bands, which influences chip segmentation and affect both the cutting forces and the surface integrity[2].

The localization of plastic deformation into ASBs is dependent on microstructural features (grain size, crystallographic orientation) [3]. As a consequence, those inputs are required to properly simulate the plastic instability and the localization phenomena. Several phenomenological constitutive models such as the Johnson-Cook model[4] are commonly used for the simulation of strain localization during metal cutting operations. Such models provide a macroscopic description of the response of a material point during cutting operations. They however fail in accounting for the possible influence of microstructural heterogeneities. In order to include the influence

of microstructure, Simoneau et al. [5] improved the Johnson-Cook model to account for the effect of the different metallurgical phases. This strategy allowed obtaining a more realistic description of the temperature field and the cutting forces at the chip level. An alternative approach consists in using the general framework of crystal plasticity to explicitly consider microstructural heterogeneities. For instance, Zhang et al. [6] have developed a 2D cutting simulation in small deformation. Tajalli et al. [7] carried out a study in large rotation and small deformation under plane strain conditions. They showed that cutting forces and chip morphology are impacted by the local crystallographic texture. A 3D crystal plasticity model has been recently developed by Ayed et al. [8] for finite transformations. According to the results, a significant evolution of the crystallographic texture is observed during cutting operations.

The main objective of the present work is to develop a thermodynamically consistent hyperelastic constitutive model to describe the thermo-mechanical behavior of the Ti17 titanium alloy. The grain shape and the crystallographic orientation are explicitly taken into account. The behavior of both the α and β phases is described using a modified crystal plasticity model coupled to a Continuum Damage Model (CDM).

This paper is organized as follows. In the first section, the hyperelastic constitutive model is detailed. The identification procedure for the two-phase $\alpha + \beta$ microstructure and the single

phase β microstructure are presented in the second section. The cutting simulation results are discussed in the third section.

2. Description of the crystal plasticity model

2.1. Kinematics

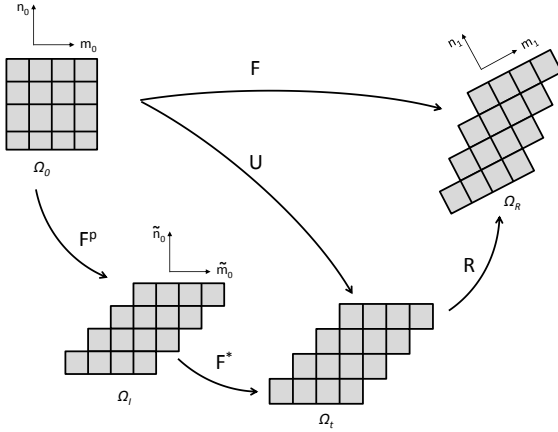


Fig. 1. Multiplicative decomposition of the deformation gradient tensor F into plastic contribution F^p , thermoelastic contribution F^* and rotation R .

We consider here an arbitrary material point for which the state at each time depends on the deformation path history. The deformation path is represented by the history of the deformation gradient tensor F . Using the polar decomposition, the deformation gradient tensor is decomposed as the product of a rotation tensor R and a stretch tensor U :

$$F = R \cdot U \quad (1)$$

The orthogonal tensor R represents the rotation, while the different effects of the deformation mechanisms are contained in the symmetric stretch tensor U . The formulation chosen here relies on the multiplicative decomposition of the stretch tensor U into an inelastic part F^p , associated with the crystallographic slip deformation, and a thermoelastic part F^* , associated with the thermoelastic deformation (see Fig.1):

$$U = F^* \cdot F^p \quad (2)$$

This formulation uses the isoclinic decomposition introduced by Lee [9] and Mandel [10] to formulate constitutive relations. As shown in Fig 1, three different configurations are therefore considered: the initial configuration Ω_0 , the intermediate configuration Ω_t and the current configuration Ω_r . For each slip system s , the intermediate configuration, which contains the undistorted lattice, allows defining the slip direction \tilde{m}_0^s and the slip plane normal \tilde{n}_0^s . The list of slip systems for the body-centered cubic (bcc) β phase and the hexagonal close-packed

(hcp) α phase is given in Table 1. For the single β phase, following the suggestions of [11, 12], only the $\langle 111 \rangle \{110\}$ and $\langle 111 \rangle \{112\}$ slip systems are considered. For the resolution of field equations resulting from equilibrium and compatibility conditions, the explicit finite element solver of ABAQUS is used. Constitutive relations are implemented within a VUMAT subroutine which uses the co-rotational stress tensor $\tilde{\sigma}$ for the description of the mechanical behavior. This stress tensor is connected to the Cauchy stress tensor σ according to:

$$\sigma = R^T \cdot \tilde{\sigma} \cdot R \quad (3)$$

2.2. State equations

At each time, the state of a material point is defined by a set of state variables, which are the thermoelastic strain tensor E^* , the absolute temperature T , the damage variable D and the isotropic hardening variables q^s associated with different slip systems. The Green-Lagrange thermoelastic strain tensor E^* , is expressed from F^* as follows:

$$E^* = \frac{1}{2} (F^{*T} \cdot F^* - I) \quad (4)$$

The state variables allow defining the specific free energy ψ , which is expressed in the intermediate configuration as follows:

$$\begin{aligned} \rho_0 \psi &= \rho_0 \psi^*(E^*, T, D) + \rho_0 \psi^p(q^s, D) \\ \rho_0 \psi &= \frac{1}{2} E^* : \mathbb{C}^*(T, D) : E^* - E^* : \mathbb{C}^*(T, D) : \alpha (T - T_0) \\ &+ \rho_0 c_p \left(T - T_0 - T \log \left(\frac{T}{T_0} \right) \right) + \frac{1}{2} Q (1 - D) \sum_s q^s \sum_t H^{st} q^t \end{aligned} \quad (5)$$

In the above equation, T_0 is a reference temperature, c_p is the specific heat, Q is the hardening modulus, H is an interaction matrix and α is the temperature-dependent thermal expansion tensor such that: $\alpha = \alpha_0 \xi(T)$. The specific free energy ψ is used as a thermodynamic potential from which the different state laws can be derived.

The second Piola-Kirchhoff stress tensor P^* is obtained using equation 5 as:

$$P^* = \rho_0 \frac{\partial \psi}{\partial E^*} = \mathbb{C}^*(T, D) : (E^* - \alpha (T - T_0)) \quad (6)$$

$\mathbb{C}^*(T, D)$ is the fourth order elastic stiffness tensor, which depends on both temperature and damage. It accounts for the elastic anisotropy of the cubic and hexagonal lattice through \mathbb{C}_0 . The dependence of the elastic stiffness tensor with respect to

Table 1. Slip systems for centred cubic and hexagonal close-packed structural material

Hexagonal close-packed (α phase)		
Name	Family	Number
Basal	$\langle 11\bar{2}0 \rangle \{0001\}$	3
Prismatic	$\langle 11\bar{2}0 \rangle \{10\bar{1}0\}$	3
Pyramidal<a>	$\langle 11\bar{2}0 \rangle \{11\bar{0}1\}$	6
Pyramidal<a+c>	$\langle 11\bar{2}3 \rangle \{10\bar{1}1\}$	12
Centred cubic (β phase)		
	$\langle 111 \rangle \{110\}$	12
	$\langle 111 \rangle \{112\}$	12

the damage and the temperature variables takes then the following form :

$$\begin{aligned} \mathbb{C}^*(T, D) = & \beta(T)H(I : -P^*)\mathbb{P}^s : \mathbb{C}_0 : \mathbb{P}^s + (1 - D)\beta(T)[\\ & H(I : P^*)\mathbb{P}^s : \mathbb{C}_0 : \mathbb{P}^s + \mathbb{P}^d : \mathbb{C}_0 : \mathbb{P}^d + \mathbb{P}^d : \mathbb{C}_0 : \mathbb{P}^s + \mathbb{P}^s : \mathbb{C}_0 : \mathbb{P}^d] \end{aligned} \quad (7)$$

\mathbb{P}^s and \mathbb{P}^d are respectively the spherical and deviatoric projection tensors and are defined as follows:

$$\mathbb{P}^s = \frac{1}{3}I \otimes I \quad (8)$$

$$\mathbb{P}^d = \mathbb{I} - \frac{1}{3}I \otimes I \quad (9)$$

H is the Heaviside function. According to (7), damage degradation affects both the spherical and the deviatoric parts of the stiffness tensor when the hydrostatic pressure $I : P^*$ is positive. At the opposite, only the deviatoric part is impacted by damage when the hydrostatic pressure $I : P^*$ is negative. This description allows accounting for closure effects. The relation between the second Piola-Kirchhoff stress tensor P^* and the Cauchy stress $\tilde{\sigma}$ is:

$$\tilde{\sigma} = \frac{1}{\det(U)} F^* \cdot P^* \cdot F^{*T} \quad (10)$$

For each slip system s , the critical shear stress r^s measures the resistance to crystallographic slip due to strain hardening. From the definition of the specific free energy ψ , one obtains that:

$$r^s = \rho_0 \frac{\partial \psi}{\partial q^s} = (1 - D) Q \sum_t H^{st} q^t \quad (11)$$

The specific entropy s , which is the thermodynamic force associated with the temperature T , is expressed as:

$$\begin{aligned} \rho_0 s = & -\rho_0 \frac{\partial \psi}{\partial T} = -\frac{1}{2} E^* : \frac{\partial \mathbb{C}^*}{\partial T} : E^* \\ & + E^* : \mathbb{C}^* : \left(\alpha + \frac{\partial \alpha}{\partial T} (T - T_0) \right) + \rho_0 c_p \ln \left(\frac{T}{T_0} \right) \end{aligned} \quad (12)$$

The thermodynamic force Y driving the development of the damage Y is given by:

$$\begin{aligned} Y = & -\rho_0 \frac{\partial \psi}{\partial D} = -\frac{1}{2} E^* : \frac{\partial \mathbb{C}^*}{\partial D} : E^* + E^* : \frac{\partial \mathbb{C}^*}{\partial D} : \alpha (T - T_0) \\ & + \frac{1}{2} Q \sum_s q^s \sum_t H^{st} q^t \end{aligned} \quad (13)$$

2.3. Evolution equations

At a given time, the specific intrinsic dissipation source d_1 is calculated from:

$$d_1 = p - \dot{\psi} - s\dot{T} \quad (14)$$

The power developed by internal forces is expressed from the co-rotational stress tensor $\tilde{\sigma}$ and the eulerian strain rate defined by $\tilde{d} = \dot{U} \cdot U^{-1}$ through the relation:

$$\rho_0 p = J \tilde{\sigma} : \tilde{d} \quad (15)$$

Using equation 5, we can obtain:

$$d_1 = \frac{1}{\rho_0} \left(M : L^p - \sum_s r^s \dot{q}^s - Y \dot{D} \right) \quad (16)$$

In the above equation, the Mandel stress tensor M , which is the power conjugate to the plastic part of the velocity gradient $L^p = \dot{F}^p \cdot F^{p-1}$, has been introduced. This stress measure is connected to P^* with:

$$M = F^{*T} \cdot F^* \cdot P^* \quad (17)$$

According to (16), some evolution equations for L^p , \dot{q}^s and \dot{D} are needed for the constitutive model to be complete. Within the crystal plasticity framework, the plastic part of the velocity

gradient tensor is conveniently written:

$$L^p = \sum_s \tilde{m}_0^s \otimes \tilde{n}_0^s \dot{\gamma}^s \quad (18)$$

where $\dot{\gamma}^s$ is the plastic shear strain rate on slip system s . For the plastic flow rule, a modified version of the model of (Meriç and Caillaud [13]) is used. Based on dislocation theory [14], the modification has been introduced to account for the effect of dislocation multiplication and/or annihilation on the flow behavior:

$$\dot{\gamma}^s = (q^s)^2 \left\langle \frac{|\tau^s| - r^s}{K} \right\rangle^n \text{sign}(\tau^s) \quad (19)$$

where $\tau^s = M : (m^s \otimes n^s)$ is the shear stress acting on slip system s . K and n are a viscosity parameters. Q and b are the isotropic hardening rule material parameters. q_0 denotes the initial dislocation density. For the evolution of damage, a power type of relation is used:

$$\dot{D} = \left\langle \frac{Y}{Y_r} \right\rangle^m \|L^p\| (1 - D) \quad (20)$$

Y_r is a material parameter which measures the resistance to damage development and m is a rate sensitivity parameter. In the above equations, K , n , Q , b , Y_r and m are temperature depending parameters.

3. Parameter identification

In this section, the procedure used for the identification of material parameters for the β -rich Ti17 titanium alloy is presented. For this purpose, two different microstructures have been considered. The first microstructure is solely composed of equiaxed β grains. This microstructure is used to identify the material parameters associated with the β phase of the Ti17 alloy. The second microstructure is composed of α lamellae embedded in a β matrix. It is used for the determination of the material parameters associated with the α phase.

To determine the material parameters, some compression, shear and tension tests have been carried out using a Gleeble 3500 simulator. The experimental procedure is presented in [3]. The compression tests, which have been conducted at temperatures ranging from 25 to 900°C and strain rates ranging from 0.1 to 50 s⁻¹, have been used for the identification of the viscoplastic flow rule parameters for both phases. The shear and tension tests allow determining the parameters of the damage rule for the lamellar two-phase $\alpha + \beta$ Ti17 microstructure only. Tensile and shear tests have been conducted on specimens with different states of triaxiality (i.e. shear, smooth, notched

with a radius of 8, 4 or 2 mm) at temperatures ranging from 25 to 800°C and strain rates ranging from 0.1 to 1 s⁻¹.

For the simulation of these tests, a synthetic microstructure is first generated using the NEPER software [15]. A random crystallographic orientation is then affected to each grain. For the lamellar $\alpha + \beta$ microstructure, the crystallographic orientation of α phase lamellae is randomly selected according to the Burgers orientation relationship [16]:

$$(110)_\beta \parallel (0001)_\alpha \text{ and } [\bar{1}\bar{1}\bar{1}]_\beta \parallel [2\bar{1}10]_\alpha \quad (21)$$

Also, for the simulation, all tests are considered to be adiabatic.

3.1. Compression tests

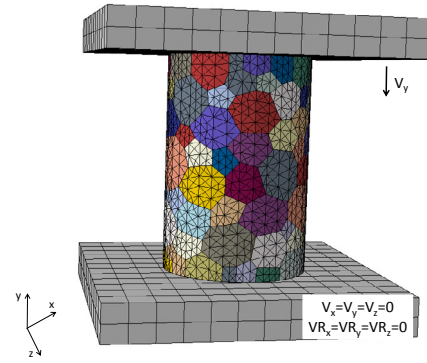


Fig. 2. Geometrical model and boundary conditions for compression tests

Fig. 2 shows the geometrical model, which contains 250 grains, used for the identification of the viscoplastic flow rule parameters. C3D4 tetrahedral elements (with 1 integration point) have been used in this section. Convergence is obtained with 170 elements/grain. The friction coefficient has been taken into account according to the proposition of [8]. The identification procedure is as follows:

- First, the identification of the β -treated Ti17 parameters is performed. This step allows obtaining an evolution function for each parameter (i.e. $K^\beta(T)$, $n^\beta(T)$, $Q^\beta(T)$ and $b^\beta(T)$).
- Then, using the identified β -treated Ti17 parameters and the experimental stress strain curves obtained for $\beta + \alpha$ Ti17, the α phase parameters (i.e. $K^\alpha(T)$, $n^\alpha(T)$, $Q^\alpha(T)$ and $b^\alpha(T)$) are identified.

Fig. 3 shows some identification results of the above parameters for the $\beta + \alpha$ and the β -treated Ti17 at different temperatures and a strain rate of 1 s⁻¹.

3.2. Tensile and shear tests

The tensile and shear tests are simulated to determine damage parameters (i.e. Y_r and m) for the $\alpha + \beta$ Ti17 alloy. The

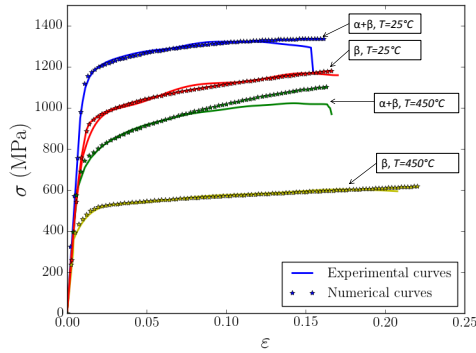


Fig. 3. Comparison between numerical and experimental stress-strain curves at different temperatures and a strain rate of 1 s^{-1} .



Fig. 4. Geometrical models and boundary conditions for tensile and shear tests

corresponding geometrical models are shown in Figure 4. Both the Y_r and m parameters have been identified for each temperature from the experimental force versus displacement curves. Figure 5 presents the identified force-displacement curves of the shear, smooth and notched specimens at the temperature of 25°C and a strain rate of 1 s^{-1} . As shown in Fig 5, an increase of stress triaxiality is associated with an increase of the maximum force and a decrease of the maximum elongation.

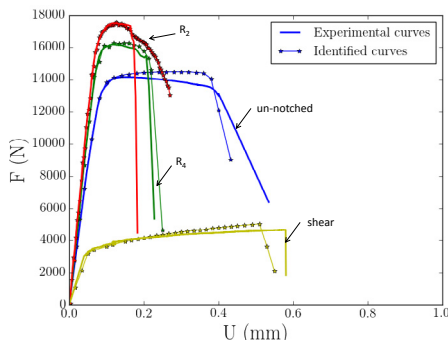


Fig. 5. Comparison between numerical and experimental force versus displacement curves for a temperature of 25°C and a strain rate of 1 s^{-1} .

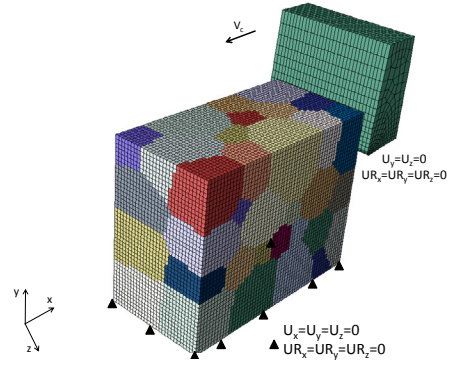


Fig. 6. Geometrical model and boundary conditions for the cutting simulation

4. Cutting simulation

In order to study the impact of microstructural features on chip segmentation, orthogonal cutting simulations have been carried out. As shown in Fig 6, the cutting model includes the tungsten carbide tool and an $\alpha + \beta$ Ti17 titanium alloy work-piece. The workpiece contains 70 grains with random crystallographic orientation. C3D8R elements have been used for this simulation. The mesh size is about $10 \times 10 \times 10 \mu\text{m}$. The geometrical model and the boundary conditions are presented in Fig 7. The cutting tool is defined as a deformed solid with an edge radius of $10 \mu\text{m}$ and with rake and flank angles of 5° . The cutting speed, the feed rate and the cutting depth are respectively $V_c = 75 \text{ m/min}$, $f = 0.1$ and 0.2 mm/rev and $a_p = 0.25 \text{ mm}$. During chip formation, the friction coefficient is constant and equal to 0.3 [8].

The experimental cutting tests used for comparison have been presented in [8]. They were conducted using a Leadwell LTC25iL CNC lathe. A Kistler 9257B piezoelectric dynamometer has been used to measure the cutting force F_c . The cutting speed and the feed rates performed are respectively $V_c = 75 \text{ m/min}$ and $f = 0.1$ and 0.2 mm/rev . The experimental cutting depth is $a_p = 5 \text{ mm}$. The average value of the experimental cutting force ranges from 1090 ± 70 to $1720 \pm 100 \text{ N}$. In this work, the experimental and numerical average values of cutting force are compared. The numerical cutting force is plotted in Fig 7. For comparison purpose, because the experimental and numerical cutting depth are different, the cutting force is assumed to vary linearly with the cutting depth a_p . As a result, the numerical cutting force is converted and compared to the experimental results with $(F_c / f a_p)$ [8]. The cutting force error between the finite element modelling (FEM) and the experimental does not exceed 8%, which means the parameter identification procedure is correct.

As shown in Fig 8, depending on the crystallographic orientation, a strain localization phenomenon, leading to the formation of an Adiabatic Shear Band (ASB), is observed. Indeed, ASBs initiate at the tool tip (in the high compressive area), then propagate along the two sides of the workpiece before reaching the top surface. The propagation along the sides of the workpiece is faster than the propagation through the thickness. In this region, the formed chip shows a strong heterogeneous dis-

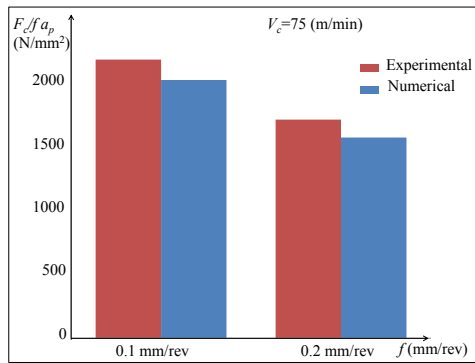


Fig. 7. Comparison between converted experimental and numerical average values of cutting force

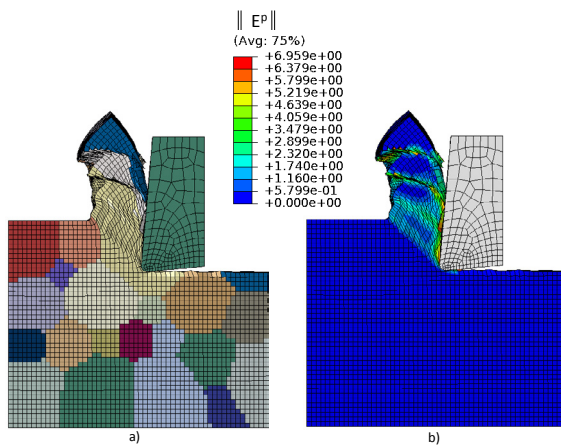


Fig. 8. Impact of the crystallographic orientation on chip segmentation: a) Deformed mesh and b) Norm of the plastic deformation.

tribution of the plastic deformation. However, when the conditions are not met for strain localization, an unsegmented chip is formed. Indeed, the plastic deformation becomes more homogeneous in the chip. As a result, when the grain size is comparable to the feed rate and/or the cutting depth, the chip segmentation is strongly impacted by the crystallographic orientation.

5. Conclusions

In this paper, a thermodynamically consistent hyperelastic constitutive model based on the crystal plasticity theory has been implemented in the ABAQUS/Explicit finite element solver with a user-defined subroutine. The flow behavior parameters have been identified from compression tests carried out on β -treated Ti17 and $\beta+\alpha$ Ti17 specimens. In addition, tensile and shear tests have been performed to calibrate the damage model.

Finally, orthogonal cutting operations have been simulated to understand the possible influence of the microstructure on chip segmentation. The cutting force is well predicted by the model. In addition, a strong dependence of the chip segmentation to the crystallographic orientation has been observed. Indeed, when the chip is fragmented, the shear bands initiate at the tool tip, then propagate along the two sides of the workpiece

to the top surface. Also, a strong heterogeneous distribution of the plastic deformation is observed in the formed chip.

References

- [1] J.D. Velasquez, B. Bolle, P. Chevrier, G. Geandier, and A. Tidu. Metallurgical study on chips obtained by high speed machining of a ti–6 wt.% al–4 wt.% v alloy. *Materials Science and Engineering: A*, 452:469–474, 2007.
- [2] H. Zhen and R. Komanduri. On a thermomechanical model of shear instability in machining. *CIRP Annals*, 44(1):69 – 73, 1995. ISSN 0007-8506. URL <http://www.sciencedirect.com/science/article/pii/S000785060762277X>.
- [3] H.B. Boubaker, Y. Ayed, C. Mareau, and G. Germain. On the formation of adiabatic shear bands in titanium alloy ti17 under severe loading conditions. *AIP Conference Proceedings*, (1):070004, 2018. URL <https://aip.scitation.org/doi/abs/10.1063/1.5034900>.
- [4] G. Johnson and W. Cook. A constitutive model and data for metals subject to large strains, high strain rates and high temperatures. *Proceedings of the 7th international symposium on ballistics*, 1983.
- [5] A. Simoneau, E. Ng, and M.A. Elbestawi. Chip formation during microscale cutting of a medium carbon steel. *International Journal of Machine Tools and Manufacture*, 46(5):467–481, 2006.
- [6] Y. Zhang, T. Mabrouki, D. Nelias, C. Courbon, J. Rech, and Y. Gong. Cutting simulation capabilities based on crystal plasticity theory and discrete cohesive elements. *Journal of Materials Processing Technology*, 212(4): 936 – 953, 2012. ISSN 0924-0136. URL <http://www.sciencedirect.com/science/article/pii/S0924013611003517>.
- [7] S.A. Tajalli, M.R. Movahhedy, and J. Akbari. Simulation of orthogonal micro-cutting of fcc materials based on rate-dependent crystal plasticity finite element model. *Computational Materials Science*, 86:79 – 87, 2014. ISSN 0927-0256. URL <http://www.sciencedirect.com/science/article/pii/S0927025614000226>.
- [8] Y. Ayed, C. Robert, G. Germain, and A. Ammar. Orthogonal micro-cutting modeling of the ti17 titanium alloy using the crystal plasticity theory. *Finite Elements in Analysis and Design*, 137:43 – 55, 2017. ISSN 0168-874X. URL <http://www.sciencedirect.com/science/article/pii/S0168874X17302093>.
- [9] E.H. Lee. Elastic-plastic deformation at finite strains. *Journal of applied mechanics*, 36(1):1–6, 1969.
- [10] J. Mandel. Equations constitutives et directeurs dans les milieux plastiques et viscoplastiques. *International Journal of Solids and Structures*, 9(6): 725–740, 1973.
- [11] A.C. Lewis, S.M. Qidwai, and A.B. Geltmacher. Slip systems and initiation of plasticity in a body-centered-cubic titanium alloy. *Metallurgical and Materials Transactions A*, 41(10):2522–2531, Oct 2010. URL <https://doi.org/10.1007/s11661-010-0284-5>.
- [12] S. Lhadi, S. Berbenni, N. Gey, T. Richeton, and L. Germain. Micromechanical modeling of the effect of elastic and plastic anisotropies on the mechanical behavior of β -ti alloys. *International Journal of Plasticity*, 109: 88 – 107, 2018. ISSN 0749-6419. URL <http://www.sciencedirect.com/science/article/pii/S0749641918301839>.
- [13] L. Meric and G. Cailletaud. Single crystal modeling for structural calculations: Part 2—finite element implementation. *Journal of Engineering Materials and Technology*, 113(1):171–182, 1991.
- [14] D. Hull and D.J. Bacon. *Introduction to Dislocations (Fifth Edition)*. Oxford, 2011. URL <https://www.sciencedirect.com/science/article/pii/B9780080966724000190>.
- [15] R. Quey, P.R. Dawson, and F. Barbe. Large-scale 3d random polycrystals for the finite element method: Generation, meshing and remeshing. *Computer Methods in Applied Mechanics and Engineering*, 200(17):1729 – 1745, 2011. ISSN 0045-7825. URL <http://www.sciencedirect.com/science/article/pii/S004578251100003X>.
- [16] S. Suri, G.B. Viswanathan, T. Neeraj, D.H. Hou, and M.J. Mills. Room temperature deformation and mechanisms of slip transmission in oriented single-colony crystals of an α/β titanium alloy. *Acta Materialia*, 47(3):1019 – 1034, 1999. ISSN 1359-6454. URL <http://www.sciencedirect.com/science/article/pii/S1359645498003644>.